One-step implementation of a nonadiabatic geometric fSim gate in superconducting circuits

M.-R. Yun,[1] Zheng Shan,[2,*] L.-L. Sun,[3] L.-L. Yan,[1,4] Y. Jia,[1,4,5,†] Shi-Lei Su,[1,4,‡] and Gang Chen[1]

[1]*School of Physics and Laboratory of Zhongyuan Light, Key Laboratory of Materials Physics of Ministry of Education, Zhengzhou University, Zhengzhou 450052, China*

[2]*State Key Laboratory of Mathematical Engineering and Advanced Computing, Zhengzhou 450001, Henan, China*

[3]*College of Physics, Tonghua Normal University, Tonghua 134000, China*

[4]*Institute of Quantum Materials and Physics, Henan Academy of Sciences, Zhengzhou 450046, China*

[5]*Key Laboratory for Special Functional Materials of Ministry of Education and School of Materials and Engineering, Henan University, Kaifeng 475001, China*

(Received 12 April 2024; accepted 25 July 2024; published 8 August 2024)

Due to their significant application in reducing algorithm depth, fSim gates have attracted a lot of attention. However, during the implementation of quantum gates, fluctuations in control parameters and decoherence caused by the environment may lead to a decrease in the fidelity of the gate. Implementing an fSim gate that is robust to these factors in one step remains an unresolved issue. In this paper, we propose a one-step implementation of a nonadiabatic geometric fSim gate composed of a nonadiabatic holonomic controlled-phase (CP) gate and a nonadiabatic noncyclic geometric ISWAP gate with parallel paths in a tunable superconducting circuit. Compared to the composite nonadiabatic geometric fSim gate composed of a nonadiabatic holonomic CP gate and a nonadiabatic geometric ISWAP gate, our scheme takes only half the time and demonstrates robustness to parameter fluctuations, as well as to environmental impacts. Moreover, the scheme does not require complex controls, making it very easy to implement in experiments, and can be achieved in various circuit structures. Our scheme may provide a promising path toward quantum computation and simulation.

DOI: 10.1103/PhysRevA.110.022608

I. INTRODUCTION

In the noisy intermediate-scale quantum (NISQ) era, the implementation of fast and high-fidelity quantum gates has great significance. Although a universal gate set can be constructed through arbitrary single-qubit gates and a nontrivial two-qubit gate [1], many algorithms demand a variety of two-qubit gates [2]. Replacing an arbitrary two-qubit gate in algorithms requires six to eight single-qubit gates and three controlled-phase (CP) gates [3]. Implementing algorithmic circuits through a series of two-qubit gates directly is of great significance for reducing circuit depth, especially using composite two-qubit quantum gates. Among the most widely used quantum gates, the fSim gate has demonstrated its superiority in many NISQ algorithms, including the quantum approximate-optimization algorithm [4], the linear-depth-circuits algorithm for simulating molecular electronic structure [5], and error-mitigation techniques [6]. Therefore, constructing fSim gates has attracted a lot of attention. A combination of an ISWAP gate and a CP gate is used to generate an fSim gate in the standard approach [7]. This leads to a waste of time and decoherence, which results in information loss or even collapse and resource waste. To ensure complete algorithms within the quantum coherence lifetime of quantum systems, one-step construction of high-fidelity fSim gates is highly anticipated.

Superconducting quantum circuits, due to their scalability, flexibility, and anharmonicity [8–11], provide a promising implementation platform for achieving high-fidelity fSim gates. Quantum information in superconducting qubits is lithographically defined. Properties of superconducting qubits such as energy levels, transition frequencies, and anharmonicity are determined by the device parameters in the circuit and can be adjusted according to demand [12]. In addition, states of superconducting qubits can be easily read through nondestructive measurement technology [13]. Superconducting qubits can be divided into different categories based on the coupling object, and they all have different circuit structures. In recent years, the transmon qubit [14] has been one of the most widely studied; it can effectively suppress charge noise and is easy to prepare, integrate, and expand [15]. However, the second excited state of transmons has a short coherence time. A cross-shaped transmon called an Xmon [16] which has the four legs of the cross is easy to couple while maintaining a high level of coherence and has attracted a lot of attention [17–21]. Recent experiments with superconducting quantum circuits have demonstrated its superiority [22–24]. In view of this, the construction of an fSim gate using superconducting Xmons is worth investigating.

During the execution of quantum operations, fluctuations of control parameters can seriously affect the fidelity of quantum gates. Since the geometric phase depends only on the global characteristics of the evolution and is immune to

*Contact author: zzzhengming@163.com
†Contact author: jiayu@zzu.edu.cn
‡Contact author: slsu@zzu.edu.cn

fluctuations of evolution paths, constructing quantum logic gates using geometric phases is seen as one of the effective means to cope with fluctuations of control parameters. In view of the above points, nonadiabatic geometric quantum computation (NGQC) [25–27] and nonadiabatic holonomic quantum computation (NHQC) [28,29] based on Abelian and non-Abelian geometric phases in two-level and three-level systems, respectively, have been proposed and have attracted a lot of attention [30–40]. However, due to the cyclic evolution conditions of geometric quantum gates, the time of geometric evolution is usually longer than that of dynamical evolution [41–44]. Recently, to shorten the evolution time, nonadiabatic noncyclic geometric quantum computation (NNGQC) was proposed and developed [45–49]; it goes beyond the limitation of the cyclic condition, making it more robust against decoherence, and it has been demonstrated in experiment [50].

Inspired by these studies, we propose a parallel geometric scheme to implement an fSim gate using the method of NNGQC in the $\{|01\rangle, |10\rangle\}$ basis and NHQC in the $\{|11\rangle, |02\rangle, |20\rangle\}$ basis, ensuring robustness against control-parameter fluctuations. In contrast to the existing theoretical and experimental schemes, the present one has the following characteristics: (1) The gate time required for our scheme with NNGQC+NHQC is half that of the composite nonadiabatic geometric quantum scheme with NGQC+NHQC and significantly less than the standard two-step fSim gate (details are given in Appendix A). This reduction in gate time implies that our scheme is more robust against decoherence caused by the environment. (2) Our scheme is robust to control error and frequency error because of its geometric features. (3) The scheme we designed does not require complex controls, making it very easy to implement in experiments, and it can be achieved in various circuit structures. Therefore, our protocol provides a promising strategy for fault-tolerant quantum computation and simulation.

This paper is organized as follows. In Sec. II, we introduce the physical model that is used to construct the fSim gate. In Sec. III, we provide a detailed parallel geometric scheme for implementing the fSim gate in one step. In Sec. IV, we represent the feasibility and superiority of our scheme through numerical simulation. In Sec. V, we show a circuit that implements the parallel geometric fSim gate with higher adjustability by adding a coupler. Finally, we provide an experimental feasibility analysis of our scheme in Sec. VI and conclude in Sec. VII.

II. PHYSICAL MODEL TO CONSTRUCT AN fSim GATE

A. fSim gate

The fSim gate, as a combination of an ISWAP gate and a CP gate [9], holds great significance for reducing circuit depth [5] and enhancing the quantum approximate optimization algorithm [4]. If we adjust the parameters, the fSim gate can perform various quantum operations, thereby simplifying quantum circuit design and making it easier to implement in practical physical systems. This versatility and ease of implementation make it a key component in the field of quantum computing. The matrix representation of an fSim gate in the

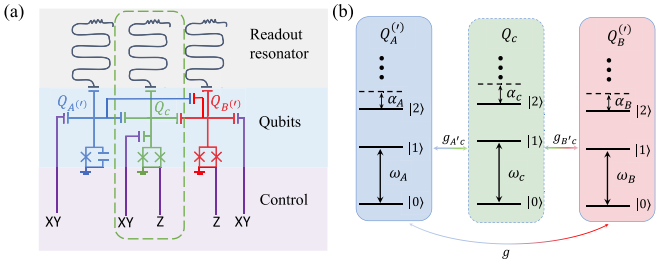

FIG. 1. (a) Circuit diagram. For direct coupling, two Xmon qubits Q_A and Q_B (blue and red) are capacitively connected via a capacitor. For indirect coupling, a coupler Q_c (green) is added. $Q_{A'}$ and $Q_{B'}$ are connected by nearest-neighbor coupling with Q_c and next-nearest-neighbor coupling with the capacitor. Single-qubit operations can be implemented by local XY control, and the frequencies of $Q_{B^{(\prime)}}$ and Q_c can be modulated by the magnetic flux with the local Z control line. Each qubit can be measured using a single readout resonator. The capacitance in the superconducting quantum interference device loop is not shown. (b) Energy structure of each qubit.

$\{|00\rangle, |01\rangle, |10\rangle, |11\rangle\}$ basis is given by [7]

$$\mathrm{fSim}(\vartheta, \Xi) = \begin{bmatrix} 1 & 0 & 0 & 0 \\ 0 & \cos\vartheta & -i\sin\vartheta & 0 \\ 0 & -i\sin\vartheta & \cos\vartheta & 0 \\ 0 & 0 & 0 & e^{i\Xi} \end{bmatrix}. \quad (1)$$

Due to the different frequency requirements of the ISWAP gate and CP gate, the fSim gate is generally implemented in two steps, which hinders the implementation of high-fidelity circuits. Moreover, the fluctuation of control parameters can also lead to a decrease in the fidelity of quantum gates. One-step implementation of robust fSim gates is of great significance for both quantum computation and quantum simulations.

B. Physical model

We now proceed to present our scheme based on superconducting circuits. The domain energy of the system is reflected in the E_J/E_C ratio. To reduce the impact of charge noise, which is more difficult to handle than flux noise, and improve the coherence of the system, $E_J \gg E_C$ should be satisfied. In addition, for the convenience of coupling, Xmon qubits are used in our scheme.

We consider two adjacent Xmons Q_A and Q_B that are capacitively connected, and the frequency of Q_B can be adjusted by the magnetic flux with the local Z control line, as shown in Fig 1(a). The Hamiltonian of this system can be described as

$$\begin{aligned} \hat{H}_s &= \hat{H}_A + \hat{H}_B + \hat{H}_{\mathrm{int}}, \\ \hat{H}_A &= 4E_{CA}\hat{n}_A^2 - E_{JA}\cos\hat{\phi}_A, \\ \hat{H}_B &= 4E_{CB}\hat{n}_B^2 - \mathcal{E}_{JB}, \\ \hat{H}_{\mathrm{int}} &= 4e^2\frac{C_g}{C_A C_B}\hat{n}_A\hat{n}_B, \end{aligned} \quad (2)$$

where $\hat{H}_A$ ($\hat{H}_B$) denotes the Hamiltonian of the individual Xmon A (B), $\hat{H}_{\mathrm{int}}$ is the interaction Hamiltonian of two Xmons, $\mathcal{E}_{JB} = E_{JBL}\cos\hat{\phi}_{BL} + E_{JBR}\cos\hat{\phi}_{BR}$, $E_{JBL(R)}$ is the energy of the left (right) Josephson junction of Q_B, $E_{CA(CB)} =$

$e^2/2C_{A(B)}$ is the charging energy of the corresponding capacitance, $\hat{n}_{A(B)} = Q_{A,(B)}/2e$ is the operator of the Cooper-pair number, $\hat{\phi}_{A(B)}$ is the reduced node flux, $E_{JA(JB)} = I_c\Phi_0/2\pi$ is the energy of the corresponding Josephson junction with $\Phi_0 = h/2e$, and I_c is the critical current of the Josephson junction.

The two quantities $\hat{n}$ and $\hat{\phi}$ obey the canonical commutation relation [51], i.e., $[\hat{\phi}, \hat{n}] = i$. With this, in the Xmon regime $E_J \gg E_C$, the Hamiltonian of Eq. (2) can be written as ($\hbar = 1$)

$$\begin{aligned}\hat{H}_A &= \omega_A \hat{a}_A^\dagger \hat{a}_A - \frac{\alpha_A}{2}\hat{a}_A^\dagger \hat{a}_A^\dagger \hat{a}_A \hat{a}_A,\\ \hat{H}_B &= \omega_B \hat{a}_B^\dagger \hat{a}_B - \frac{\alpha_B}{2}\hat{a}_B^\dagger \hat{a}_B^\dagger \hat{a}_B \hat{a}_B,\\ \hat{H}_{\rm int} &= g(\hat{a}_A^\dagger \hat{a}_B + \hat{a}_A \hat{a}_B^\dagger - \hat{a}_A^\dagger \hat{a}_B^\dagger - \hat{a}_A \hat{a}_B),\end{aligned} \tag{3}$$

where

$$\begin{aligned}\hat{a}_{A(B)}^\dagger &= \frac{1}{\sqrt{2\omega_{A(B)}}}\left(\sqrt{8E_{CA(B)}}i\hat{n}_{A(B)} + \frac{\omega_{A(B)}\hat{\phi}_{A(B)}}{\sqrt{8E_{CA(B)}}}\right),\\ \hat{a}_{A(B)} &= \frac{1}{\sqrt{2\omega_{A(B)}}}\left(-\sqrt{8E_{CA(B)}}i\hat{n}_{A(B)} + \frac{\omega_{A(B)}\hat{\phi}_{A(B)}}{\sqrt{8E_{CA(B)}}}\right),\\ \omega_{A(B)} &= \sqrt{8E_{JA(B)}E_{CA(B)}} - E_{CA(B)},\\ \alpha_{A(B)} &= E_{CA(B)}, \quad g = \frac{1}{2}\frac{C_{AB}}{\sqrt{C_A C_B}}\sqrt{\omega_A \omega_B}.\end{aligned} \tag{4}$$

The energy structure of each qubit is shown in Fig. 1(b). The Hamiltonian under the rotating-wave approximation (RWA) including levels with two excitations for the system in Fig. 1 can be written as

$$\hat{H}_1 = \begin{bmatrix} \omega_{00} & 0 & 0 & 0 & 0 & 0\\ 0 & \omega_{01} & 0 & g & 0 & 0\\ 0 & 0 & \omega_{02} & 0 & \sqrt{2}g & 0\\ 0 & g & 0 & \omega_{10} & 0 & 0\\ 0 & 0 & \sqrt{2}g & 0 & \omega_{11} & \sqrt{2}g\\ 0 & 0 & 0 & 0 & \sqrt{2}g & \omega_{20}\end{bmatrix} \tag{5}$$

in the $\{|00\rangle, |01\rangle, |02\rangle, |10\rangle, |11\rangle, |20\rangle\}$ basis, where the bare state of Xmons A and B is denoted as $|n_A n_B\rangle = |n_A\rangle \otimes |n_B\rangle$ ($n_i \in 0, 1, 2$). We can observe that there is coupling between $|01\rangle$ and $|10\rangle$ as well as between $|11\rangle$ $|02\rangle$ and $|20\rangle$ simultaneously, so it is possible to achieve both ISWAP and CP gates simultaneously.

III. PARALLEL IMPLEMENTATION OF THE fSim GATE WITH NNGQC+NHQC

The fSim gate is a combination of an ISWAP gate and a CP gate. Generally speaking, implementing ISWAP gates and implementing CP gates in superconducting circuits require different conditions. When implementing the ISWAP gate, it is usually necessary to have two frequencies of two logical qubits equal to each other to achieve resonance between $|01\rangle$ and $|10\rangle$. However, when implementing the CP gate, the frequency of $|11\rangle$ needs to be equal to $|02\rangle$ or $|20\rangle$; i.e., the frequency difference between $|01\rangle$ and $|10\rangle$ needs to be α. Therefore, the fSim gates are generally completed in two steps. In this section, we will introduce how to simultaneously implement these two two-qubit gates in one step.

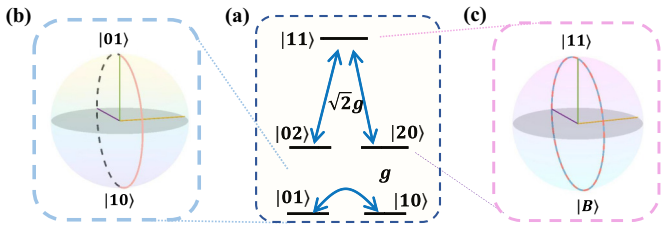

FIG. 2. (a) Energy-level diagrams of the double-excitation manifold and the single-excitation manifold in the case of direct coupling when performing the fSim gate. Bloch-sphere representation of the relevant energy in (b) the single-excitation manifold and (c) the two-excitation manifold.

To implement the fSim gate in one step, three energy levels of each transmon are considered, and the parameters of transmons can be set as $\omega_A = \omega_B$ and $\alpha_A = \alpha_B$; the energy-level structure and coupling are shown in Fig. 2(a). To achieve simultaneous evolution of single-excitation subspace and two-excitation subspace and accelerate gate speed, the coupling strength does not need to be much smaller than the anharmonicity. Additionally, during the preparation process, the level anharmonicity of each qubit is solely related to the energy of the capacitor, making it easy to achieve equality. However, it is very challenging to make the frequencies of two qubits completely equal. Therefore, Xmon B is designed with a tunable frequency. The $|0\rangle_B \to |1\rangle_B$ transition frequency of Q_B as a function of flux bias is shown in Appendix. C.

A. NHQC implementation of the CP part

First, we will demonstrate how to obtain a nonadiabatic holonomic phase on $|11\rangle$ [30,32]. When $\omega_{20} = \omega_{02}$, the interaction between $|11\rangle$, $|02\rangle$, and $|20\rangle$ can be regarded as a three-level structure with the same detuning. Under these parameter conditions, after the rotating frame with transform operator $V(t) = \exp[-i(\omega_{11}|11\rangle\langle 11| + \omega_{02}|02\rangle\langle 02| + \omega_{20}|20\rangle\langle 20|)t]$ is applied, ignoring rapidly oscillating terms in the RWA, the Hamiltonian (5) can be written as

$$\hat{H}_2 = \Delta|11\rangle\langle 11| + 2g(|11\rangle\langle B| + \text{H.c.}), \tag{6}$$

with $\Delta = \alpha_A = \alpha_B$ and $|B\rangle = \frac{1}{\sqrt{2}}(|02\rangle + |20\rangle)$. There is a dark state $|D\rangle = \frac{1}{\sqrt{2}}(|02\rangle - |20\rangle)$ of Eq. (6) which is decoupled from the system completely. We set

$$\Delta = 2\Omega\sin\gamma, \quad g = \tfrac{1}{2}\Omega\cos\gamma. \tag{7}$$

Then,

$$\begin{aligned}\hat{H}_2 = {}& \Omega\sin\gamma(|11\rangle\langle 11| + |B\rangle\langle B|) + \Omega[\cos\gamma|B\rangle\langle 11| + \text{H.c.}]\\ & + \Omega\sin\gamma(|11\rangle\langle 11| - |B\rangle\langle B|).\end{aligned} \tag{8}$$

Only states $|11\rangle$ and $|B\rangle$ are coupled; in the basis of $|11\rangle$ and $|B\rangle$, we can map $|11\rangle\langle 11| + |B\rangle\langle B| \to \mathbb{I}$, $|11\rangle\langle B| + |B\rangle\langle 11| \to \sigma_x$, $|11\rangle\langle 11| - |B\rangle\langle B| \to \sigma_z$, where $\mathbb{I}$ is the identity matrix and σ_x and σ_z are the Pauli matrices. Based on this,

$$\hat{H}_2 = \Omega\sin\gamma\,\mathbb{I} + \Omega(\cos\gamma\sigma_x + \sin\gamma\sigma_z). \tag{9}$$

When the evolution time $\tau = \pi/\Omega$, the evolution operator of the three-level system can be represented as

$$U_2(\tau,\ 0) = e^{-i\phi}|B\rangle\langle B| + e^{i\phi}|11\rangle\langle 11| + |D\rangle\langle D|, \quad (10)$$

where $\phi = \pi \sin\gamma$. After undergoing a cycle of evolution with $\tau_2 = 2\pi/(16g^2 + \Delta^2)$, $|11\rangle$ in the computational subspace will obtain a geometric phase.

Next, we will examine whether this evolution is holonomic; the holonomy transformation should satisfy two conditions: (1) the evolution of the subspace is cyclic, and (2) there is no dynamical phase in this cyclic evolution. For condition 1, in the subspace spanned by $\{|B\rangle,\ |11\rangle\}$, from the evolution operator in Eq. (10), we can see condition 1 is satisfied. For condition 2, $\langle m|\hat{H}_2|r\rangle$, where $m, r \in \{11, B\}$, is easy to verify. That is to say, the gate in subspace $\{|11\rangle, |02\rangle, |20\rangle\}$ is a holonomic gate.

B. NNGQC implementation of the ISWAP part

At the same time, under this parameter set, $|01\rangle$ and $|10\rangle$ can achieve resonance interaction; the energy-level structure and coupling are shown in Fig. 2(a). To obtain tunable coupling between $|01\rangle \leftrightarrow |10\rangle$, the flux bias can be set as magnetic flux [52], and the frequency of Xmon B in Appendix C can be rewritten in the form

$$\omega_B(t) = \omega_B + \epsilon \sin(\nu t + \varphi), \quad (11)$$

where ν and φ indicate the frequency and phase of the modulated field, respectively. Then, using the Jacobi-Anger identity,

$$\exp[i\beta\cos(\nu t + \varphi)] = \sum_{m=-\infty}^{+\infty} i^m J_m(\beta)\exp[im(\nu t + \varphi)], \quad (12)$$

with $J_m(\beta)$ being Bessel functions of the first kind with $\beta = \epsilon/\nu$.

When $\Delta = \omega_A - \omega_B = \nu$, the Hamiltonian in the bases $|01\rangle$ and $|10\rangle$ with RWA in the interaction picture can be written as

$$\hat{H}_r = \begin{pmatrix} 0 & \mathcal{G}\, e^{-i(\varphi-\pi/2)} \\ \mathcal{G}\, e^{i(\varphi-\pi/2)} & 0 \end{pmatrix}, \quad (13)$$

where $\mathcal{G} = J_1(\beta)g$.

To shorten the evolution time, we will now use the method of NNGQC to implement the ISWAP part. We choose a set of auxiliary states

$$|\phi_1(t)\rangle = \cos\frac{\alpha(t)}{2}e^{-i\frac{\eta}{2}}|01\rangle + \sin\frac{\alpha(t)}{2}e^{i\frac{\eta}{2}}|10\rangle,$$
$$|\phi_2(t)\rangle = \sin\frac{\alpha(t)}{2}e^{i\frac{\eta}{2}}|01\rangle - \cos\frac{\alpha(t)}{2}e^{i\frac{\eta}{2}}|10\rangle. \quad (14)$$

Then, we insert them into the von Neumann equation [53],

$$\dot{\Pi}_m(t) = -i[H(t), \Pi_m(t)], \quad (15)$$

where $\Pi_m(t) = |\phi_m(t)\rangle\langle\phi_m(t)|$. Then, we can get restriction equations for two Hamiltonian parameters,

$$\mathcal{G} = \frac{\dot{\alpha}}{2\sin[\varphi(t) - \pi/2 - \eta(t)]},$$
$$\varphi(t) = \eta(t) - \arctan\left[\frac{\dot{\alpha}(t)\cot[\chi(t)]}{\dot{\eta}(t)}\right] + \frac{\pi}{2}. \quad (16)$$

The evolution operator is

$$U_r(T,0) = e^{i\Upsilon}|\phi_1(T)\rangle\langle\phi_1(0)| + e^{-i\Upsilon}|\phi_2(T)\rangle\langle\phi_2(0)|$$
$$= \begin{pmatrix} e^{i\frac{\eta_-}{2}}(\cos\gamma\cos\frac{\alpha_-}{2} + i\cos\frac{\alpha_+}{2}\sin\gamma) & e^{-i\frac{\eta_+}{2}}(-\cos\gamma\sin\frac{\alpha_-}{2} + i\sin\frac{\alpha_+}{2}\sin\gamma) \\ e^{i\frac{\eta_+}{2}}(\cos\gamma\sin\frac{\alpha_-}{2} + i\sin\frac{\alpha_+}{2}\sin\gamma) & e^{i\frac{\eta_-}{2}}(\cos\gamma\cos\frac{\alpha_-}{2} - i\cos\frac{\alpha_+}{2}\sin\gamma) \end{pmatrix}, \quad (17)$$

where $\alpha_\pm = \alpha(T) \pm \alpha(0)$, $\eta_\pm = \eta(T) \pm \eta(0)$, and $\Upsilon = \gamma_d + \gamma_g$ is the total phase, which including a geometric phase, $\gamma_g = i\int_0^T \langle\phi_1|\dot{\phi}_1\rangle \mathrm{dt} = \int_0^T \frac{1}{2}\dot{\eta}\cos\chi\,\mathrm{dt}$, and a dynamical one, $\gamma_d = -\int_0^T \langle\phi_1|\hat{H}_r|\phi_1\rangle \mathrm{dt} = -\int_0^T \mathcal{G}\cos\alpha(\mathrm{t})\cos[\varphi(\mathrm{t}) - \pi/2 - \eta(\mathrm{t})]\mathrm{dt}$. To obtain a pure geometric phase, we set $\varphi(t) - \eta(t) = 0$. Therefore, the total phase $\Upsilon = \gamma_g = \int_{\eta(0)}^{\eta(T)}\int_{\alpha(0)}^{\alpha(T)} \frac{1}{2}\sin\alpha d\alpha d\eta$ is half of the solid angle enclosed by the trajectory and the geodesic connecting the initial and final points [45]. When $\eta_+ = -\pi, \eta_- = 0, \alpha_+ = 0, \alpha_- = -\pi$, and $\gamma = \pi$, ISWAP operation can be obtained, and the evolution time of such a nonadiabatic noncyclic process is $\tau_1 = \pi/2\mathcal{G}$.

C. Implementation of the fSim gate with parallel paths

In order to obtain both evolutions simultaneously, it is only necessary to satisfy the evolution time $n_1 \times \tau_1 = n_2 \times \tau_2$, with $n_1,\ n_2 \in N_+$ (N_+ represents the set of positive integer natural numbers). To minimize the impact of decoherence by minimizing the evolution time as much as possible, we have selected $n_1 = 1$ and $n_2 = 2$; that is to say, $\alpha_A = \alpha_B = 4\sqrt{3}\mathcal{G}$, i.e., $T = \tau_1 = 2\tau_2$. More specifically, $|11\rangle$ undergoes two cycles to obtain nonadiabatic holonomic phase 2ϕ, and at the same time, $|01\rangle$ and $|10\rangle$ complete nonadiabatic noncyclic geometric ISWAP interaction. These evolutions can be described on the Bloch sphere as Figs. 2(b) and 2(c). It is worth noting that these two paths evolve simultaneously. And if one sets different values of detuning Δ and coupling strength $\mathcal{G}$, $|11\rangle$ can obtain different phases φ. To better represent two parallel evolutions, we plot the populations of $|10\rangle$, $|01\rangle$, and $|11\rangle$ of the initial state at $\frac{1}{\sqrt{2}}(|10\rangle + |11\rangle)$ in Fig. 3. The population colors for each state correspond to the colors in the Bloch spheres in Figs. 2(b) and 2(c).

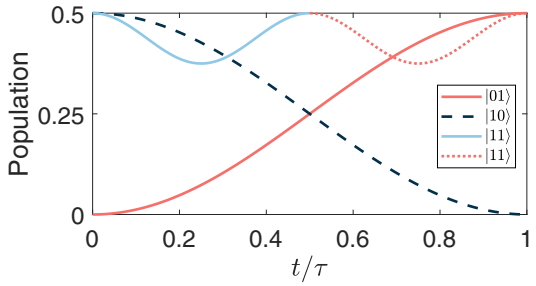

FIG. 3. Numerical simulation of the fSim gate population corresponding to the NNGQC+NHQC scheme. The blue solid line and red dotted line represent the population of $|11\rangle$ for the first and second cycles, and the red solid line and black dashed line show the populations of $|01\rangle$ and $|10\rangle$ (the decoherence caused by the environment is not considered in this simulation).

IV. GATE PERFORMANCE

To fully analyze the feasibility of our scheme, we define the average fidelity as

$$\mathcal{F} = \frac{1}{4\pi^2}\int_0^{2\pi}\int_0^{2\pi}\langle\psi_f|\rho|\psi_f\rangle d\theta_1 d\theta_2, \tag{18}$$

where the initial state $|\psi(0)\rangle = (\cos\theta_1|0\rangle_1 + \sin\theta_1|1\rangle_1)\otimes(\cos\theta_2|0\rangle_2 + \sin\theta_2|1\rangle_2)$ (the initial state is normalized), $|\psi_f\rangle$ is the ideal final state, and the density matrix of this system can be solved by the Lindblad master equation

$$\dot{\rho}(t) = i\,[\rho(t), \hat{H}_s] + \sum_{j=1}^{2}\left[\frac{\kappa_-^j}{2}\mathcal{L}(\sigma_j) + \frac{\kappa_z^j}{2}\mathcal{L}(\chi_j)\right], \tag{19}$$

where $\mathcal{L}(\mathcal{A}) = 2\mathcal{A}\rho\mathcal{A}^\dagger - \mathcal{A}^\dagger\mathcal{A}\rho - \rho\mathcal{A}^\dagger\mathcal{A}$ is the Lindblad operator for operator $\mathcal{A}$, κ_-^j and κ_z^j are the relaxation and dephasing rates of the jth Xmon, and $\sigma_j = |j'-1\rangle\langle j'|$ and $\chi_{j'} = |j'\rangle\langle j'|$, with $j \in \{1,\ 2\}$ and $j' \in \{0,\ 1,\ 2\}$, for the j'th level of the jth Xmon. From Fig. 4, we can see the average fidelities of the NNGQC+NHQC method and conventional NGQC+NHQC (detailed in Appendix D) can reach 0.9998 and 0.9997, respectively. Next, we will demonstrate the robustness of our scheme based on the NGQC+NHQC and

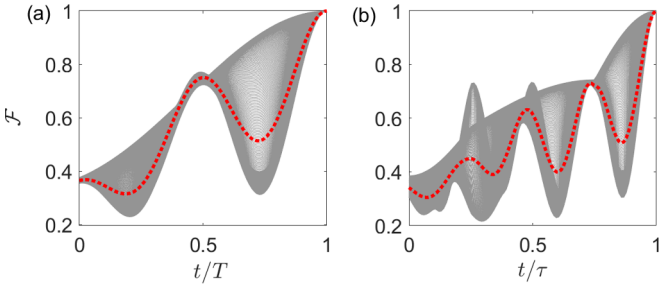

FIG. 4. Numerical simulation of the average fidelity $\mathcal{F}$ of the fSim gate with (a) NNGQC+NHQC and (b) NGQC+NHQC. The gray lines represent the fidelity of 500 different initial states, and the red dotted line expresses the average fidelity of these 500 initial states. The parameter settings are as follows: $g = 1$, $\alpha = 4\sqrt{3}$, $\omega_A = \omega_B = 100$, and $\kappa_-^j = \kappa_z^j = 10^{-4}$.

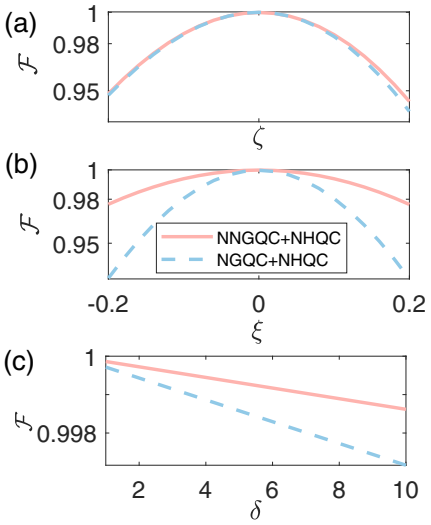

FIG. 5. The performance of the fSim gate under parameter fluctuation. Numerical simulation of the average fidelity $\mathcal{F}$ of the fSim gate under (a) the coupling-strength error ζ, (b) the frequency fluctuation of Xmon B ξ, and (c) the decay (dephasing) rate δ.

NNGQC+NHQC methods to coupling-strength errors and the frequency fluctuation of Xmon B. We assume the coupling strength between Xmons A and B varies in the range of $\mathcal{G} \to (1+\zeta)\mathcal{G}$, with $\zeta \in [-0.2, 0.2]$, and $\omega_B \to (1+\xi)\omega_B$, with $\xi \in [-0.2, 0.2]$. Furthermore, we also simulate the average fidelity as a function of the relaxation rate and dephasing rate of the jth Xmon $\kappa_-^j = \kappa_z^j \to \delta\kappa_-^j = \delta\kappa_z^j$, with $\delta \in [1, 10]$. From Fig. 5, we can see that even with a 20% fluctuation in coupling strength $\mathcal{G}$, the fidelity of the two schemes can still remain above 0.93, and for the frequency fluctuation of Xmon B and the environment noise, the NNGQC+NHQC method showed greater superiority.

In addition, leakage error is another source of infidelity in superconducting systems. We have utilized the characteristic that superconducting qubits can leak from low energy levels to high energy levels to achieve the ISWAP gate and CP gate simultaneously. Despite considering leakage at higher energy levels, the fSim gate can still maintain high fidelity. This is discussed in detail in Appendix B.

V. CAPACITIVE COUPLING VIA COUPLER

The process of adjusting the qubit frequency may lead to an issue named "frequency crowding" and control crosstalk. Although the use of asymmetric transmons can help alleviate this problem, the impact of this issue still exists. A tunable coupler can help alleviate this problem [54]. Moreover, after adding a tunable coupler, the coupler strength of two logical qubits can be adjusted between exactly 0 and over 100 MHz (absolute value); that is, the coupling can be turned on and off by adjusting the coupler frequency ω_c. Here, we will demonstrate that our scheme can be performed in the circuit with a tunable coupler. Similar to the case of direct coupling, the Hamiltonian can be written in a form consistent with

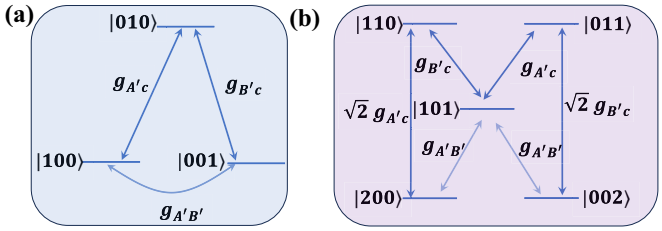

FIG. 6. Energy-level diagrams of (a) the single-excitation manifold and (b) the double-excitation manifold when performing the fSim gate. Blue double-headed arrows denote exchange interactions between the energy levels. The arrow color of $g_{A'B'}$ is lighter than the others to indicate the coupling of the nearest neighbor is stronger than the coupling of the next-nearest neighbor.

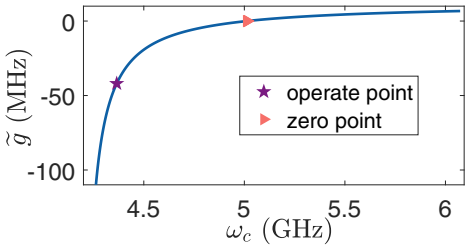

FIG. 7. The effective coupling strength $\tilde{g}$ varies the frequency of the coupler ω_c. At the point marked by a pentagram, the same coupling as for direct coupling can be achieved. At the point marked by a triangle, the coupling between two logical qubits can be turned off.

Eq. (3),

$$\hat{H}_{s'} = \hat{H}_{A'} + \hat{H}_{B'} + \hat{H}_c + \hat{H}_{\mathrm{int}'},$$
$$\hat{H}_{j'} = \omega_{j'}\hat{a}^\dagger_{j'}\hat{a}_{j'} - \frac{\alpha_{j'}}{2}\hat{a}^\dagger_{j'}\hat{a}^\dagger_{j'}\hat{a}_{j'}\hat{a}_{j'}$$
$$\hat{H}_{\mathrm{int}'} = \sum_{j'<k'} g_{j'k'}(\hat{a}^\dagger_{j'}\hat{a}_{k'} + \hat{a}_{j'}\hat{a}^\dagger_{k'} - \hat{a}^\dagger_{j'}\hat{a}^\dagger_{k'} - \hat{a}_{j'}\hat{a}_{k'}),$$

where $j', k' \in \{A', B', c\}$ and we set $A' < B' < c$ and $\omega_{j'}$ is the transition frequency from the ground state to the first excited state for the jth Xmon. Based on the actual situation, we consider that the system is at most doubly excited, and the energy-level diagram is shown in Fig. 6.

To directly demonstrate the coupling between logical qubits, when $\omega_{j'} \gg g_{j'k'}$, we can adopt the Schrieffer-Wolff transformation [55]

$$\hat{U} = \sum_{m=A',B'}\left[\frac{g_{mc}}{\omega_m - \omega_c}(\hat{a}^\dagger_m\hat{a}_c - \hat{a}_c\hat{a}^\dagger_m) - \frac{g_m}{\omega_m + \omega_c}(\hat{a}^\dagger_m\hat{a}^\dagger_c - \hat{a}_m\hat{a}_c)\right]; \quad (20)$$

then, keeping all terms to second order, we have

$$\tilde{\hat{H}} = e^{\hat{U}}\hat{H}_{s'}(e^{\hat{U}})^\dagger = \sum_m \tilde{\omega}'_m\hat{a}^\dagger_m\hat{a}_m - \frac{\tilde{\alpha}_m}{2}\hat{a}^\dagger_m\hat{a}^\dagger_m\hat{a}_m\hat{a}_m + \tilde{g}(\hat{b}^\dagger_{A'}\hat{b}_{B'} + \hat{b}_{A'}\hat{b}^\dagger_{B'}), \quad (21)$$

where

$$\tilde{g} \approx \frac{g_{A'c}g_{B'c}}{2}\sum_m\left(\frac{1}{\omega_m - \omega_c} - \frac{1}{\omega_m + \omega_c}\right) + g_{A'B'},$$
$$\tilde{\omega}_m \approx \omega_m + g^2_{mc}\left(\frac{1}{\omega_m - \omega_c} - \frac{1}{\omega_m + \omega_c}\right),$$
$$\tilde{\alpha}_m \approx \alpha_m. \quad (22)$$

In this approximation, we assume that the coupler is always in the ground state. We rotate the Hamiltonian into the interaction picture, and after using the RWA and second-order perturbation approximation, it can be observed that there is still only coupling between two logical qubits. The effective coupling strength $\tilde{g}$ varies the frequency of the coupler ω_c between two logical qubits and is shown in Fig. 7. At the point marked by a purple pentagram, the same coupling as direct coupling can be achieved; that is to say, after adding a tunable coupler, the above scheme can still be achieved.

VI. EXPERIMENTAL FEASIBILITY

In order to examine the feasibility of this scheme in the experiment, we now discuss the relevant parameters, which are shown in Table I. Based on these settings, the decay rate and the dephasing rate of each Xmon $\kappa^j_- = \kappa^j_z = 2\pi \times 4.18$ kHz. Based on these settings, the effective coupling strength between Xmons A and B is $\mathcal{G} = 2\pi \times 41.8$ MHz. Considering the Bessel functions of the first kind, $\nu = 0.369$ and $\epsilon = 0.692$, from Fig. 8(a), it can be seen that the coupling strength between Xmons A and B is $g = 71.92$ MHz. Furthermore, as shown in Fig. 8(b), when the magnetic flux bias is adjusted to ± 0.3153, the frequency condition can be satisfied. The device parameters are demonstrated in Table I. For the NGQC+NHQC and NNGQC+NHQC methods, the gate time is 23.92 and 11.96 ns, respectively. These parameters are reasonable.

VII. CONCLUSION

In conclusion, we proposed a scheme to implement a geometric fSim gate with parallel paths in one step in a superconducting circuit. Our scheme protects the fSim gate from the control error due to the intrinsic robustness of the geometric phase and mitigates decoherence caused by the environment by shortening the evolution time with the parallel paths. Furthermore, implementing the composite two-qubit gate in one step significantly reduces the circuit depth in quantum simulation. Additionally, our scheme does not require complex controls, making it straightforward to implement in

TABLE I. Device parameters.

	Q_A	Q_c	Q_B
$E_c/2\pi$ (GHz)	0.3	0.12	0.3
$E_j/2\pi$ (GHz)	8.3627	30	10
		10	2.8
$\omega/2\pi$ (GHz)	4.18	[4.262, 6.076]	[3.857, 5.241]
$\alpha/2\pi$ (MHz)	300	120	300

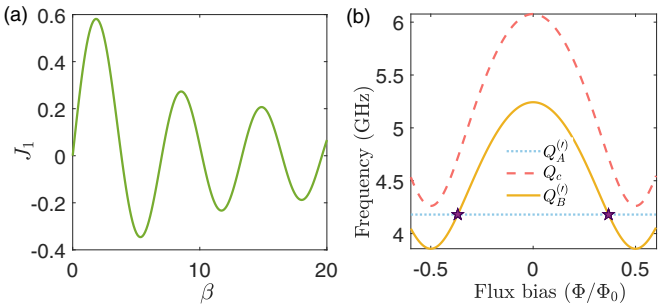

FIG. 8. (a) The Bessel function of the first kind varying with β. (b) The $|0\rangle \rightarrow |1\rangle$ transition frequencies of the logical qubit (yellow solid line and blue dotted line) and the coupler (red dashed line) varying with the flux bias Φ/Φ_0. Relevant parameters are shown in Table I.

experiments and adaptable to various circuit structures. Therefore, our scheme may provide a significant reference and pave an alternative path for implementing low-depth fSim-gate-based quantum simulations in superconducting circuits.

ACKNOWLEDGMENTS

This work was supported by the National Natural Science Foundation of China under Grants No. 12274376, No. U21A20434, and No. 12074346, a major science and technology project of Henan Province under Grant No. 221100210400, the Natural Science Foundation of Henan Province under Grants No. 232300421075 and No. 212300410085, and the Cross-Disciplinary Innovative Research Group Project of Henan Province under Grant No. 232300421004.

APPENDIX A: THE TWO-STEP IMPLEMENTATION OF fSim GATE

Here, we will demonstrate how to use a two-step scheme to construct a fSim gate.

(1) Adjust the frequency of $|01\rangle$ to be equal to $|01\rangle$, i.e., $\omega_B = \omega_A$. In order to minimize leakage errors as much as possible, we have reduced the coupling strength to half of NNGQC+NHQC in the main text, that is, $g_2 = \mathcal{G}/2$. After RWA, the effective Hamiltonian in the $\{|01\rangle, |10\rangle\}$ basis can be written as

$$\hat{H}_1 = \begin{pmatrix} 0 & g_2 \\ g_2 & 0 \end{pmatrix}, \tag{A1}$$

making the evolution time $T_1 = (\pi/2)/g_2$ to implement the ISWAP gate.

(2) Adjust the frequency of $|11\rangle$ to be equal to $|02\rangle$, i.e., $\omega_B = \omega_A + \alpha_B$. After RWA, the effective Hamiltonian in the $\{|11\rangle, |02\rangle\}$ basis becomes

$$\hat{H}_2 = \begin{pmatrix} 0 & \sqrt{2}g_2 \\ \sqrt{2}g_2 & 0 \end{pmatrix}, \tag{A2}$$

making the evolution time $T_2 = (\pi/\sqrt{2})/g_2$ to implement the CP gate.

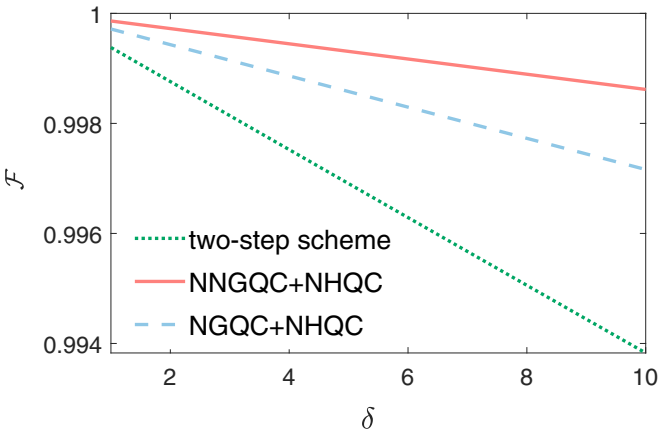

FIG. 9. The average fidelity $\mathcal{F}$ varies the decay (dephasing) rate δ. Parameters are the same as those in Fig. 5. The green dotted line represents the two-step scheme, the red solid line represents the NNGQC+NHQC scheme, and the blue dashed line represents the NGQC+NHQC scheme.

Next, we simulate the average fidelity of the two-step scheme for the fSim gate while varying the decay (dephasing) rate, where $\kappa_-^j = \kappa_z^j \rightarrow \delta\kappa_-^j = \delta\kappa_z^j$ (Fig. 9). We can see that the NNGQC+NHQC method has stronger robustness to decoherence caused by the environment.

APPENDIX B: LEAKAGE

Here, we simulate the possibility of qubits leaking into the three-excitation subspace, where the annihilation operator in the Hamiltonian is $\hat{a} = \hat{a}^\dagger = |0\rangle\langle 1| + \sqrt{2}|1\rangle\langle 2| + \sqrt{3}|2\rangle\langle 3|$ and energy levels in the Lindblad operator change to $j' \in \{0, 1, 2, 3\}$. The average fidelity is simulated in Fig. 10. We can observe that, considering decoherence and dephasing, the average fidelity of the fSim gate can still reach 0.999.

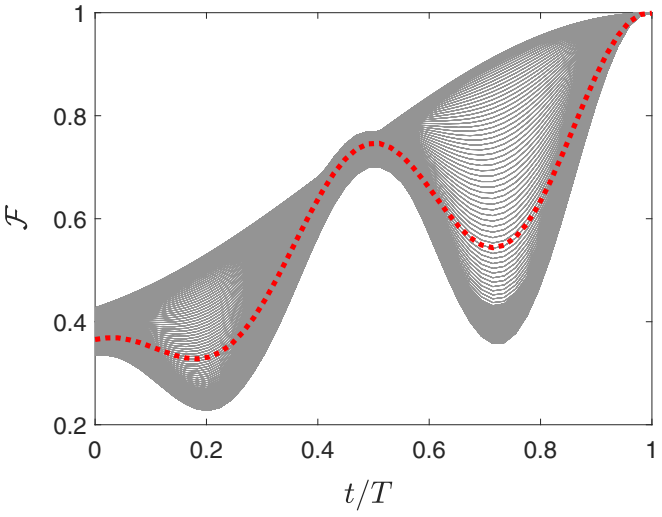

FIG. 10. The average fidelity $\mathcal{F}$ varies with evolution time when considering that the energy levels involved are the ground state, first excited state, and second excited state. Parameters are the same as those in Fig. 5.

APPENDIX C: ADJUSTABLE RANGE OF QUBIT FREQUENCY

Here, we demonstrate how to adjust the qubit frequency by adjusting the magnetic flux passing through the superconducting quantum interference device (SQUID).

Taking Q_B as an example, the energy of the tunable Josephson energy can be described as

$$\begin{aligned}
E_{JB} &= E_{JBL}\cos\phi_{BL} + E_{JBR}\cos\phi_{BR} \\
&= E_{JBL}\cos\left(\frac{\phi_{BL}+\phi_{BR}}{2}+\frac{\phi_{BL}-\phi_{BR}}{2}\right) + E_{JBR}\cos\left(\frac{\phi_{BL}+\phi_{BR}}{2}-\frac{\phi_{BL}-\phi_{BR}}{2}\right) \\
&= E_{JBL}\left(\cos\frac{\phi_{BL}+\phi_{BR}}{2}\cos\frac{\phi_{BL}-\phi_{BR}}{2}-\sin\frac{\phi_{BL}+\phi_{BR}}{2}\sin\frac{\phi_{BL}-\phi_{BR}}{2}\right) \\
&\quad + E_{JBR}\left(\cos\frac{\phi_{BL}+\phi_{BR}}{2}\cos\frac{\phi_{BL}-\phi_{BR}}{2}+\sin\frac{\phi_{BL}+\phi_{BR}}{2}\sin\frac{\phi_{BL}-\phi_{BR}}{2}\right) \\
&= (E_{JBL}+E_{JBR})\left[\cos\frac{\phi_{BL}-\phi_{BR}}{2}\cos\frac{\phi_{BL}+\phi_{BR}}{2}\right] + (E_{JBR}-E_{JBL})\left[\sin\frac{\phi_{BL}-\phi_{BR}}{2}\sin\frac{\phi_{BL}+\phi_{BR}}{2}\right] \\
&= E_{JB\Sigma}\left[\cos\frac{\pi\Phi}{\Phi_0}\cos\phi + d\sin\frac{\pi\Phi}{\Phi_0}\sin\phi\right] \\
&= E_{JB\Sigma}\cos\frac{\pi\Phi}{\Phi_0}\sqrt{1+d^2\tan^2\frac{\pi\Phi}{\Phi_0}}\cos(\phi-\phi_0),
\end{aligned} \tag{C1}$$

where $E_{JB\Sigma} = E_{JBL} + E_{JBR}$, $(\phi_{BL}+\phi_{BR})/2 = \phi$, $\Phi_0 = h/2e$ is the superconducting flux quantum, $d = (E_{JBL}-E_{JBR})/(E_{JBL}+E_{JBR})$, $\tan\phi_0 = d\tan(\pi\Phi/\Phi_0)$, Φ is the magnetic flux passing through the SQUID, and $\phi_{JBL}-\phi_{JBR} = 2\pi n + 2\pi\Phi/\Phi_0$, with $n \in N_+$.

Therefore, the frequency of Q_B is $\omega_B = \sqrt{8E_{JB}E_{CB}} - E_{CB}$. To better search for the physical quantities required for the experiment, we plot the frequency, which varies with magnetic flux bias Φ/Φ_0.

APPENDIX D: NGQC IMPLEMENTATION OF THE ISWAP PART

In this Appendix, we present the details of implementing the ISWAP part with conventional NGQC. We take the two-dimensional orthogonal eigenstates

$$|\Psi_+(t)\rangle = \cos\frac{\theta(t)}{2}|01\rangle + \sin\frac{\theta(t)}{2}e^{i\chi(t)}|10\rangle, \quad |\Psi_-(t)\rangle = \sin\frac{\theta(t)}{2}e^{i\chi(t)}|01\rangle - \cos\frac{\theta(t)}{2}|10\rangle \tag{D1}$$

as our evolution states. To ensure the geometry of this evolution, the cyclic condition and the parallel-transport condition are required,

$$|\Psi_+(T)\rangle = e^{-i\gamma}|\Psi_+(0)\rangle, \quad |\Psi_-(T)\rangle = e^{i\gamma}|\Psi_-(0)\rangle, \quad \langle\Psi_\pm(t)|\hat{H}_r(t)|\Psi_\pm(t)\rangle = 0; \tag{D2}$$

that is, $|\Psi_\pm\rangle$ can reach geometric phases $\pm\gamma$ without any dynamic phase at time T.

The evolution operator can be denoted as

$$U_r(T) = e^{i\gamma}|\Psi_+(0)\rangle\langle\Psi_+(0)| + e^{-i\gamma}|\Psi_-(0)\rangle\langle\Psi_+(0)| = \begin{pmatrix}\cos\gamma - i\cos\theta\sin\gamma & -ie^{i\chi}\sin\gamma\sin\theta \\ -ie^{i\chi}\sin\gamma\sin\theta & \cos\gamma + i\cos\theta\sin\gamma\end{pmatrix}, \tag{D3}$$

where $\theta \equiv \theta(0)$ and $\chi \equiv \chi(0)$. When $\theta = \pi/2$, $\chi(0) = 0$, and $\gamma = \pi/2$, an ISWAP evolution between $|01\rangle$ and $|10\rangle$ can be obtained, with the coupling strength $\mathcal{G}$ and ϕ satisfying

$$\begin{aligned}
&\int_0^{T_1}\mathcal{G}\mathrm{dt} = \pi/4, \quad \chi(t) = \pi/2, \quad t\in[0,T_1], \quad \int_{T_1}^{T_2}\mathcal{G}\mathrm{dt} = \pi/2, \quad \chi(\mathrm{t}) = \pi, \quad \mathrm{t}\in[\mathrm{T}_1,\mathrm{T}_2], \\
&\int_{T_2}^{T}\mathcal{G}\mathrm{dt} = \pi/4, \quad \chi(t) = \pi/2, \quad t\in[T_2,T].
\end{aligned} \tag{D4}$$

[1] A. Barenco, C. H. Bennett, R. Cleve, D. P. DiVincenzo, N. Margolus, P. Shor, T. Sleator, J. A. Smolin, and H. Weinfurter, Elementary gates for quantum computation, Phys. Rev. A **52**, 3457 (1995).

[2] J. Preskill, Quantum computing in the NISQ era and beyond, Quantum **2**, 79 (2018).

[3] N. Khaneja and S. J. Glaser, Cartan decomposition of $SU(2^n)$ and control of spin systems, Chem. Phys. **267**, 11 (2001).

[4] L. Zhou, S.-T. Wang, S. Choi, H. Pichler, and M. D. Lukin, Quantum approximate optimization algorithm: Performance, mechanism, and implementation on near-term devices, Phys. Rev. X **10**, 021067 (2020).

[5] I. D. Kivlichan, J. McClean, N. Wiebe, C. Gidney, A. Aspuru-Guzik, G. K.-L. Chan, and R. Babbush, Quantum simulation of electronic structure with linear depth and connectivity, Phys. Rev. Lett. **120**, 110501 (2018).

[6] A. Kandala, K. Temme, A. D. Córcoles, A. Mezzacapo, J. M. Chow, and J. M. Gambetta, Error mitigation extends the computational reach of a noisy quantum processor, Nature (London) **567**, 491 (2019).

[7] B. Foxen *et al.* (Google AI Quantum), Demonstrating a continuous set of two-qubit gates for near-term quantum algorithms, Phys. Rev. Lett. **125**, 120504 (2020).

[8] M. Kjaergaard, M. E. Schwartz, J. Braumüller, P. Krantz, J. I.-J. Wang, S. Gustavsson, and W. D. Oliver, Superconducting qubits: Current state of play, Annu. Rev. Condens. Matter Phys. **11**, 369 (2020).

[9] F. Arute, K. Arya, R. Babbush, D. Bacon, J. C. Bardin, R. Barends, R. Biswas, S. Boixo, F. G. S. L. Brandao, D. A. Buell, B. Burkett, Y. Chen, Z. Chen, B. Chiaro, R. Collins, W. Courtney, A. Dunsworth, E. Farhi, B. Foxen, A. Fowler, Quantum supremacy using a programmable superconducting processor, Nature (London) **574**, 505 (2019).

[10] P. Jurcevic, A. Javadi-Abhari, L. S Bishop, I. Lauer, D. F. Bogorin, M. Brink, L. Capelluto, O. Günlük, T. Itoko, N. Kanazawa, A. Kandala, G. A. Keefe, K. Krsulich, W. Landers, E. P. Lewandowski, D. T. McClure, G. Nannicini, A. Narasgond, H. M. Nayfeh, E. Pritchett, Demonstration of quantum volume 64 on a superconducting quantum computing system, Quantum Sci. Technol. **6**, 025020 (2021).

[11] M. Gong, S. Wang, C. Zha, M.-C. Chen, H.-L. Huang, Y. Wu, Q. Zhu, Y. Zhao, S. Li, S. Guo, H. Qian, Y. Ye, F. Chen, C. Ying, J. Yu, D. Fan, D. Wu, H. Su, H. Deng, H. Rong, K. Zhang, Quantum walks on a programmable two-dimensional 62-qubit superconducting processor, Science **372**, 948 (2021).

[12] J. M. Martinis, M. H. Devoret, and J. Clarke, Energy-level quantization in the zero-voltage state of a current-biased Josephson junction, Phys. Rev. Lett. **55**, 1543 (1985).

[13] V. B. Braginsky and F. Y. Khalili, Quantum nondemolition measurements: The route from toys to tools, Rev. Mod. Phys. **68**, 1 (1996).

[14] J. Koch, T. M. Yu, J. Gambetta, A. A. Houck, D. I. Schuster, J. Majer, A. Blais, M. H. Devoret, S. M. Girvin, and R. J. Schoelkopf, Charge-insensitive qubit design derived from the Cooper pair box, Phys. Rev. A **76**, 042319 (2007).

[15] J. M. Fink, Quantum nonlinearities in strong coupling circuit QED, Ph. D. thesis, ETH Zurich, 2010.

[16] R. Barends, J. Kelly, A. Megrant, D. Sank, E. Jeffrey, Y. Chen, Y. Yin, B. Chiaro, J. Mutus, C. Neill, P. O'Malley, P. Roushan, J. Wenner, T. C. White, A. N. Cleland, and J. M. Martinis, Coherent Josephson qubit suitable for scalable quantum integrated circuits, Phys. Rev. Lett. **111**, 080502 (2013).

[17] R. Barends *et al.*, Superconducting quantum circuits at the surface code threshold for fault tolerance, Nature (London) **508**, 500 (2014).

[18] J. Kelly, R. Barends, A. G. Fowler, A. Megrant, E. Jeffrey, T. C. White, D. Sank, J. Y. Mutus, B. Campbell, Yu Chen, Z. Chen, B. Chiaro, A. Dunsworth, I.-C. Hoi, C. Neill, P. J. J. OMalley, C. Quintana, P. Roushan, A. Vainsencher, and J. Wenner, State preservation by repetitive error detection in a superconducting quantum circuit, Nature (London) **519**, 66 (2015).

[19] Z.-B. Yang, P.-R. Han, X.-J. Huang, W. Ning, H. Li, K. Xu, D. Zheng, H. Fan, and S.-B. Zheng, Experimental demonstration of entanglement-enabled universal quantum cloning in a circuit, npj Quantum Inf. **7**, 44 (2021).

[20] W. Ning, R.-H. Zheng, Y. Xia, K. Xu, H. Li, D. Zheng, H. Fan, F. Wu, Z.-B. Yang, and S.-B. Zheng, Revealing inherent quantum interference and entanglement of a Dirac particle, npj Quantum Inf. **9**, 99 (2023).

[21] X. Pan, X. Cao, W. Wang, Z. Hua, W. Cai, X. Li, H. Wang, J. Hu, Y. Song, D.-L. Deng, C.-L. Zou, R.-B. Wu, and L. Sun, Experimental quantum end-to-end learning on a superconducting processor, npj Quantum Inf. **9**, 18 (2023).

[22] S.-P. Wang, A. Ridolfo, T. Li, S. Savasta, F. Nori, Y. Nakamura, and J. Q. You, Probing the symmetry breaking of a light-matter system by an ancillary qubit, Nat. Commun. **14**, 4397 (2023).

[23] P. Zhao, Z. Dong, Z. Zhang, G. Guo, D. Tong, and Y. Yin, Experimental realization of nonadiabatic geometric gates with a superconducting Xmon qubit, Sci. China: Phys. Mech. Astron. **64**, 250362 (2021).

[24] K. Luo, W. Huang, Z. Tao, L. Zhang, Y. Zhou, J. Chu, W. Liu, B. Wang, J. Cui, S. Liu, F. Yan, M.-H. Yung, Y. Chen, T. Yan, and D. Yu, Experimental realization of two qutrits gate with tunable coupling in superconducting circuits, Phys. Rev. Lett. **130**, 030603 (2023).

[25] S.-L. Zhu and Z. D. Wang, Implementation of universal quantum gates based on nonadiabatic geometric phases, Phys. Rev. Lett. **89**, 097902 (2002).

[26] W. Xiang-Bin and M. Keiji, Nonadiabatic conditional geometric phase shift with NMR, Phys. Rev. Lett. **87**, 097901 (2001).

[27] P. Z. Zhao, X.-D. Cui, G. F. Xu, E. Sjöqvist, and D. M. Tong, Rydberg-atom-based scheme of nonadiabatic geometric quantum computation, Phys. Rev. A **96**, 052316 (2017).

[28] E. Sjöqvist, D. M. Tong, L. M. Andersson, B. Hessmo, M. Johansson, and K. Singh, Non-adiabatic holonomic quantum computation, New J. Phys. **14**, 103035 (2012).

[29] G. F. Xu, J. Zhang, D. M. Tong, E. Sjöqvist, and L. C. Kwek, Nonadiabatic holonomic quantum computation in decoherence-free subspaces, Phys. Rev. Lett. **109**, 170501 (2012).

[30] E. Sjöqvist, Nonadiabatic holonomic single-qubit gates in off-resonant λ systems, Phys. Lett. A **380**, 65 (2016).

[31] E. Herterich and E. Sjöqvist, Single-loop multiple-pulse nonadiabatic holonomic quantum gates, Phys. Rev. A **94**, 052310 (2016).

[32] G. F. Xu, C. L. Liu, P. Z. Zhao, and D. M. Tong, Nonadiabatic holonomic gates realized by a single-shot implementation, Phys. Rev. A **92**, 052302 (2015).

[33] G. F. Xu, D. M. Tong, and E. Sjöqvist, Path-shortening realizations of nonadiabatic holonomic gates, Phys. Rev. A **98**, 052315 (2018).

[34] P. Shen, Y. Liang, T. Chen, and Z.-Y. Xue, Accelerated super-robust nonadiabatic holonomic quantum gates, Phys. Rev. A **108**, 032601 (2023).

[35] B.-J. Liu, L.-L. Yan, Y. Zhang, M.-H. Yung, S.-L. Su, and C. X. Shan, Decoherence-suppressed nonadiabatic holonomic quantum computation, Phys. Rev. Res. **5**, 013059 (2023).

[36] P. Z. Zhao, X. Wu, and D. M. Tong, Dynamical-decoupling-protected nonadiabatic holonomic quantum computation, Phys. Rev. A **103**, 012205 (2021).

[37] S. Li and Z.-Y. Xue, Dynamically corrected nonadiabatic holonomic quantum gates, Phys. Rev. Appl. **16**, 044005 (2021).

[38] L.-N. Sun, L.-L. Yan, S.-L. Su, and Y. Jia, One-step implementation of time-optimal-control three-qubit nonadiabatic holonomic controlled gates in Rydberg atoms, Phys. Rev. Appl. **16**, 064040 (2021).

[39] F.-Q. Guo, J.-L. Wu, X.-Y. Zhu, Z. Jin, Y. Zeng, S. Zhang, L.-L. Yan, M. Feng, and S.-L. Su, Complete and nondestructive distinguishment of many-body Rydberg entanglement via robust geometric quantum operations, Phys. Rev. A **102**, 062410 (2020).

[40] B.-B. Liu, Z. Shan, M.-R. Yun, D.-Y. Wang, B.-J. Liu, L.-L. Yan, M. Feng, and S.-L. Su, Robust three-qubit search algorithm in Rydberg atoms via geometric control, Phys. Rev. A **106**, 052610 (2022).

[41] S. Olmschenk, R. Chicireanu, K. D. Nelson, and J. V. Porto, Randomized benchmarking of atomic qubits in an optical lattice, New J. Phys. **12**, 113007 (2010).

[42] T. Xia, M. Lichtman, K. Maller, A. W. Carr, M. J. Piotrowicz, L. Isenhower, and M. Saffman, Randomized benchmarking of single-qubit gates in a 2D array of neutral-atom qubits, Phys. Rev. Lett. **114**, 100503 (2015).

[43] Y. Wang, X. Zhang, T. A. Corcovilos, A. Kumar, and D. S. Weiss, Coherent addressing of individual neutral atoms in a 3D optical lattice, Phys. Rev. Lett. **115**, 043003 (2015).

[44] Y. Wang, A. Kumar, T.-Y. Wu, and D. S. Weiss, Single-qubit gates based on targeted phase shifts in a 3D neutral atom array, Science **352**, 1562 (2016).

[45] B.-J. Liu, S.-L. Su, and M.-H. Yung, Nonadiabatic noncyclic geometric quantum computation in Rydberg atoms, Phys. Rev. Res. **2**, 043130 (2020).

[46] N. Eivarsson and E. Sjöqvist, Genuinely noncyclic geometric gates in two-pulse schemes, Phys. Rev. A **108**, 032612 (2023).

[47] M.-R. Yun, F.-Q. Guo, L.-L. Yan, E. Liang, Y. Zhang, S.-L. Su, C. X. Shan, and Y. Jia, Parallel-path implementation of nonadiabatic geometric quantum gates in a decoherence-free subspace with nitrogen-vacancy centers, Phys. Rev. A **105**, 012611 (2022).

[48] L.-N. Sun, F.-Q. Guo, Z. Shan, M. Feng, L.-L. Yan, and S.-L. Su, One-step implementation of Rydberg nonadiabatic noncyclic geometric quantum computation in decoherence-free subspaces, Phys. Rev. A **105**, 062602 (2022).

[49] Z.-Y. Chen, J.-H. Liang, Z.-X. Fu, H.-Z. Liu, Z.-R. He, M. Wang, Z.-W. Han, J.-Y. Huang, Q.-X. Lv, and Y.-X. Du, Single-pulse two-qubit gates for Rydberg atoms with noncyclic geometric control, Phys. Rev. A **109**, 042621 (2024).

[50] J. W. Zhang, L.-L. Yan, J. C. Li, G. Y. Ding, J. T. Bu, L. Chen, S.-L. Su, F. Zhou, and M. Feng, Single-atom verification of the noise-resilient and fast characteristics of universal nonadiabatic noncyclic geometric quantum gates, Phys. Rev. Lett. **127**, 030502 (2021).

[51] U. Vool and M. Devoret, Introduction to quantum electromagnetic circuits, Int. J. Circuit Theory Appl. **45**, 897 (2017).

[52] J. Chu, D. Li, X. Yang, S. Song, Z. Han, Z. Yang, Y. Dong, W. Zheng, Z. Wang, X. Yu, D. Lan, X. Tan, and Y. Yu, Realization of superadiabatic two-qubit gates using parametric modulation in superconducting circuits, Phys. Rev. Appl. **13**, 064012 (2020).

[53] B.-J. Liu, X.-K. Song, Z.-Y. Xue, X. Wang, and M.-H. Yung, Plug-and-play approach to nonadiabatic geometric quantum gates, Phys. Rev. Lett. **123**, 100501 (2019).

[54] F. Yan, P. Krantz, Y. Sung, M. Kjaergaard, D. L. Campbell, T. P. Orlando, S. Gustavsson, and W. D. Oliver, Tunable coupling scheme for implementing high-fidelity two-qubit gates, Phys. Rev. Appl. **10**, 054062 (2018).

[55] S. Bravyi, D. P. DiVincenzo, and D. Loss, Schrieffer-Wolff transformation for quantum many-body systems, Ann. Phys. **326**, 2793 (2011).